RMetS
Royal Meteorological Society

Foehn warming distributions in nonlinear and linear flow regimes: a focus on the Antarctic Peninsula

Andrew D. Elvidge,[a]* Ian A. Renfrew,[a] John C. King,[b] Andrew Orr[b] and Tom A. Lachlan-Cope[b]
[a]*School of Environmental Sciences, University of East Anglia, Norwich, UK*
[b]*British Antarctic Survey, Cambridge, UK*

*Correspondence to: A. D. Elvidge, Centre for Ocean and Atmospheric Sciences, School of Environmental Sciences, University of East Anglia, NR4 7TJ Norwich, UK. E-mail: a.elvidge@uea.ac.uk

The structure of lee-side warming during foehn events is investigated as a function of cross-barrier flow regime linearity. Two contrasting cases of westerly flow over the Antarctic Peninsula (AP) are considered – one highly nonlinear, the other relatively linear. Westerly flow impinging on the AP provides one of the best natural laboratories in the world for the study of foehn, owing to its maritime setting and the Larsen C Ice Shelf (LCIS) providing an expansive, homogeneous and smooth surface on its east side. Numerical simulations with the Met Office Unified Model (at 1.5 km grid size) and aircraft observations are utilized. In case A, relatively weak southwesterly cross-Peninsula flow and an elevated upwind inversion dictate a highly nonlinear foehn event, with mountain wave breaking observed. The consequent strongly accelerated downslope flow leads to high-amplitude warming and ice-shelf melt in the immediate lee of the AP. However this foehn warming diminishes rapidly downwind due to upward ascent of the foehn flow via a hydraulic jump. In case C, strong northwesterly winds dictate a relatively linear flow regime. There is no hydraulic jump and strong foehn winds are able to flow at low levels across the entire ice shelf, mechanically mixing the near-surface flow, preventing the development of a strong surface inversion and delivering large fluxes of sensible heat to the ice shelf. Consequently, in case C ice-melt rates are considerably greater over the LCIS as a whole than in case A. Our results imply that although nonlinear foehn events cause intense warming in the immediate lee of mountains, linear foehn events will commonly cause more extensive lee-side warming and, over an ice surface, higher melt rates. This has major implications for the AP, where recent east-coast warming has led to the collapse of two ice shelves immediately north of the LCIS.

Key Words: foehn; Larsen Ice Shelf; gravity wave breaking; hydraulic jump; Met Office Unified Model; melt rates

Received 28 February 2014; Revised 15 October 2014; Accepted 22 October 2014; Published online in Wiley Online Library 13 December 2014

1. Introduction

The Antarctic Peninsula (AP) has been identified as one of the fastest warming regions on Earth since 1950 (Vaughan *et al.*, 2003). During this period east-coast ice shelves have been in a state of decline (Cook and Vaughan, 2010), the Larsen A and B ice shelves collapsing in spectacular fashion in 1995 and 2002, respectively (Vaughan and Doake, 1996; Rignot *et al.*, 2004). Indeed, during the summer melt season, warming near the northern tip of the AP on the east coast has been considerably greater than that on the west coast (∼0.7 and ∼0.2 K per decade respectively; Marshall *et al.*, 2006). This amplified east-coast warming has been attributed to a strengthening of westerly flow across the AP, leading to more frequent (or more intense) foehn winds above the ice shelves to the east of the AP – the so-called 'foehn hypothesis' for east coast AP warming (Marshall *et al.*, 2006; Orr *et al.*, 2008; van Lipzig *et al.*, 2008; King *et al.*, 2008; Elvidge *et al.*, 2014, hereafter E2014). The WMO (1992) defines foehn as '*a wind warmed and dried by descent, in general on the lee side of a mountain*'. Although commonly associated with high wind speeds, in this study the term is used to describe any warm, dry downslope flow.

During foehn events lee-side temperatures rise and humidities fall relative to upwind conditions. This foehn 'anomaly' is due to several mechanisms (e.g. Whiteman, 2000; Ólafsson, 2005): the drawdown of potentially warmer air from aloft; precipitation resulting in irreversible latent heating over the mountains; mechancial mixing of the stably stratified airmass over the

mountains resulting in a warming of the low-level flow; and radiative warming as a result of the dry, commonly cloud-free foehn conditions (the 'foehn clearance'; Hoinka, 1985). In an Eulerian sense, lee-side air is warmed due to: (i) the *advection* of warm foehn air replacing cooler air; (ii) *mechanical mixing* driven by lee-side turbulence, causing enhanced downward sensible heat flux in a statically stable atmosphere; and (iii) *solar warming*, either directly via radiation or indirectly via radiative warming of the surface affecting the surface energy balance. Although there has been considerable attention drawn to the variation of downslope wind speeds (e.g. Smith, 1985; Durran, 1986; Lilly, 1978; Durran, 1990; Colle and Mass, 1998), little consideration has been given to the distribution of lee-side warming during foehn events.

The Orographic Flows and Climate of the Antarctic Peninsula (OFCAP) project was designed to investigate various aspects of the foehn hypothesis for east-coast AP warming. An intensive OFCAP field campaign took place between January and February 2011 and included measurements made with an instrumented aircraft based at the British Antarctic Survey's Rothera Research Station (see Figure 1(a) for location). This study makes use of these aircraft observations and a high-resolution model to investigate two contrasting cases of westerly foehn flow on the Larsen C Ice Shelf (LCIS; Figure 1(a)). Extending ∼200 km east of the AP into the Weddell Sea, the LCIS is the largest remaining ice shelf attached to the AP and provides a flat, low friction surface comprising very few orographic or surface complexities. Indeed because of this homogeneous lee-side surface, together with the AP's isolated, maritime location and form (a relatively straight, continuous, high-level ridge; Figure 1), the study region affords relatively simple investigation of the fundamental character and dynamics of foehn flows in the absence of many of the orographic and surface complexities that characterize other more extensively studied mountain ranges such as the Alps or the Rockies. Despite this, there is of course an element of orographic heterogeneity along the length of the AP (Figure 1(c)). Although its crest does not fall below 1000 m, there are lower sections of the ridge and passes between peaks. Large glacial valleys (for example Whirlwind Inlet; WI) on the east coast of the AP provide conduits through which gap flows (Mayr *et al.*, 2007) are channelled, resulting in the propagation of foehn jets over the LCIS. The nature of these jets and the mechanisms responsible for their cause and characteristics are investigated in E2014 using aircraft observations and numerical weather prediction simulations. Gap-flow-forced foehn winds associated with severe warming have also been observed and modelled elsewhere in Antarctica – in the McMurdo Dry Valleys (Speirs *et al.*, 2010; Steinhoff *et al.*, 2013) – where too a range of foehn-associated features are found, such as lee-side acceleration, hydraulic jumps and wave breaking.

Novel observations, the use of a high-resolution model and the relative orographic simplicity of the AP (a 'natural laboratory'), allows this article to provide, in companionship with E2014, new insight into the nature and dynamics of real foehn events. It affords (as far as we are aware) the first in-depth analysis of foehn warming structure – in particular the spatial distribution of warming – and how it varies depending on the major mode of foehn variability, i.e. the linearity of the flow regime. Such knowledge starts to provide new insights into the role of foehn winds in the break up of the LCIS.

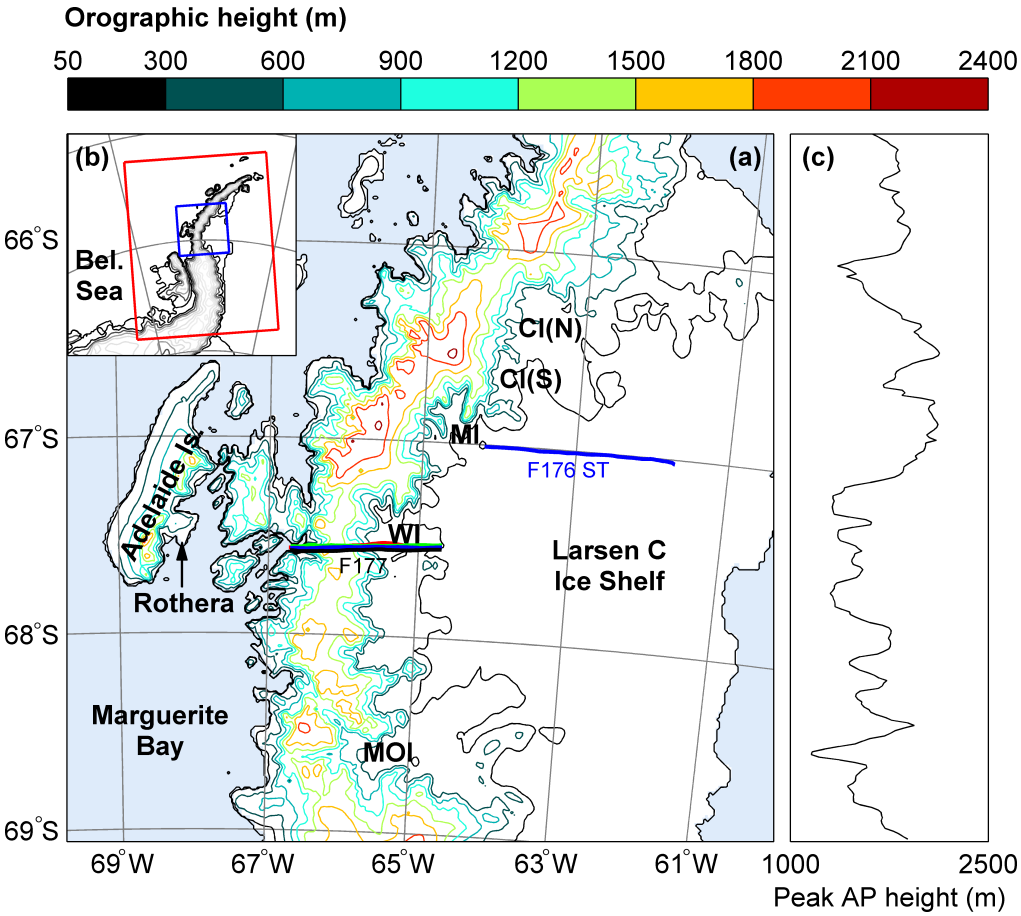

Figure 1. (a) Land mask and topographic map from MetUM 1.5 km orography data (contours, spaced at 300 m) of the section of the Antarctic Peninsula (AP) relevant to this study. The sawtooth leg from flight 176 is marked in blue and the flight 177 legs across the AP in the vicinity of Whirlwind Inlet are marked (overlaying each other) using the same colour code as in Figure 10. The sea is shaded pale blue. Key locations are marked, including: MOI, Mobil Oil Inlet; WI, Whirlwind Inlet; MI, Mill Inlet; CI (N/S), Cabinet Inlet (North/South). (b) Inset map showing the AP (and the Bellingshausen Sea to the west), the MetUM 4 km domain (red, outer box) and the MetUM 1.5 km standard domain (blue, inner box). (c) Peak AP height for each model grid point along the *y*-axis (roughly N–S). Note that passes in the crest line generally coincide with inlets on the eastern slopes of the AP.

Section 2 provides a brief theoretical overview of flow-regime linearity in the context of foehn warming, section 3 describes the data and the methods employed, section 4 presents the synoptic situation and upwind conditions associated with each case, and section 5 describes and explains the lee-side responses; the differences in foehn-warming structure and associated cross-Peninsula dynamics. Section 6 briefly compares the performance of the model with 1.5 and 4 km horizontal grid sizes. Section 7 discusses the impact on the surface energy balance and melt rates on the LCIS. Finally, the conclusions and implications of the study are presented in section 8.

2. Theoretical context: flow-regime linearity

The nature of the lee-side response to cross-barrier flow is largely dependent on the shape and height of the mountain barrier, and the characteristics of the approaching flow (Smith, 1979). A relevant parameter is therefore the non-dimensional mountain height, $\hat{h} = Nh/U$, a measure of flow linearity, where N is the Brunt–Väisälä frequency of the undisturbed upwind air mass, h is the height of the mountain and U is the wind-speed component of the undisturbed upwind flow directed towards and, in the case of an elongated barrier such as the AP, perpendicular to the barrier (e.g. Smith, 1980; Hunt and Snyder, 1980; Trombetti and Tampieri, 1987). Variables N and U must be obtained at a distance at least that of the Rossby radius of deformation, $\lambda_R = Nh/f$ (where f is the Coriolis parameter) upwind of the barrier (upwind of λ_R the flow does not 'feel' the mountains; Orr *et al.*, 2008).

In the case of a statically stable atmosphere in which N and U vary little with height, when $\hat{h} \ll 1$ the solutions obtained from linear theory are qualitatively accurate (Smith, 1980). In such cases, the flow of air over the mountain creates a disturbance whereby potentially cool dense air is forced to rise above its environmental equilibrium level. Such a disturbance generates internal gravity waves, for which the restoring force is buoyancy. Gravity waves may propagate vertically or horizontally, depending on the vertical structure of the atmosphere (Smith, 1979). The major direction of wave energy propagation is in the same direction as the near-surface disturbance, i.e. upwards, and, so long as the mountain is of sufficient along-wind length, vertically propagating waves are generated (Smith, 1979).

As $\hat{h}$ increases, the amplitude of the disturbance of the mountain on the flow increases. In the case of a stationary orographic gravity wave, linear theory breaks down when the orographically induced horizontal wind perturbation u' equals the background flow U somewhere over the barrier (Smith, 1980). Consequently strongly stratified, slowly moving flow approaching a high mountain (such that $\hat{h} > 1$) will lead to nonlinear phenomena such as upwind flow blocking, mountain wave breaking, downslope windstorms and lee-side hydraulic jumps. Such nonlinear phenomena are associated with turbulent dissipation, which acts to decelerate the cross-barrier flow. In the transition from a linear (low drag) to nonlinear (high drag) flow regime, low-level mountain wave breaking and flow blocking are thought to precede the development of a downslope windstorm and subsequent hydraulic jump. In the presence of mountain wave breaking, vertical wave propagation is curtailed due to the occurrence of a region of flow stagnation above the mountain (Smith and Grønås, 1993). Such a region is known as a wave-induced critical level as it is a result of the steepening of waves to the extent that the wave overturns, inducing turbulent dissipation (Clark and Peltier, 1977). This occurs when the wave's amplitude becomes large relative to its vertical wavelength. A wave-induced critical level is thought to act as a reflective surface for mountain waves, incurring a resonant response and leading to wave amplification in the lower troposphere, and hence the occurrence of a downslope windstorm (Peltier and Clark, 1983; Smith, 1985; Durran, 1990; Smith and Skyllingstad, 2005). Hydraulic theory explains severe downslope winds as a transition from *subcritical* (internal Froude number, $Fr > 1$) to *supercritical* ($Fr < 1$) flow over a mountain barrier in a nonlinear regime, downwind of which an abrupt readjustment to ambient, subcritical conditions occurs at some point above the lee slope in the form of a hydraulic jump (Long, 1953; Durran, 1990). Here Fr is defined following Long (1953).

Although a useful diagnostic in assessing the linearity of a cross-mountain flow regime, recall $\hat{h}$ itself is only one measure of linearity, and considers only a continuous atmosphere (i.e. constant upwind N and U with height). Vertical variations in U or N have major implications for the ensuing flow regime (Scorer, 1949; Klemp and Lilly, 1975); in particular elevated inversions have been shown to promote nonlinear flow characteristics (Brinkmann, 1974; Durran, 1986; Colle and Mass, 1998).

3. Data and methods

3.1. Observations and modelling

Aircraft measurements were made as part of the OFCAP field campaign by a De Havilland Canada Twin Otter aircraft, equipped with the Meteorological Airborne Science Instrumentation (MASIN; for further information see King *et al.*, 2008; Fiedler *et al.*, 2010). Meteorological observations relevant to this study include three-dimensional winds using a Best Aircraft Turbulence (BAT, Garman *et al.*, 2006) probe, and static pressure and total temperature using Rosemount sensors. Data from two MASIN flights are used (Natural Environment Research Council *et al.*, 2014), both of which are during case A: flight 176 during the early morning of 5 February 2011 and flight 177 during the late morning to early afternoon of the same day. Note that E2014 investigates this same case with flight 176 and three other flights.

The Met Office's Unified Model (MetUM; Davies *et al.*, 2005) Version 7.6 has been used for this study. The MetUM's dynamical core employs a non-hydrostatic, fully compressible, deep atmosphere with a semi-implicit, semi-Lagrangian, predictor-corrector scheme to solve the equations of motion. The MetUM employs Arakawa C-grid staggering in the horizontal and a Charney-Phillips grid in the vertical. The model levels are terrain-following near the surface, but become increasingly level with height.

For each case the highest resolution model used had a horizontal grid size of 1.5 km. Such a high resolution is deemed necessary to adequately resolve the complex flow field and large vertical velocities common in this area due to the AP's steep and complex orography. The model employs 70 vertical levels, which includes 8 levels below 500 m. The lowest model level is 5 m, which is lower than that recommended by Zängl *et al.* (2008), who found an improvement in model representation of Alpine foehn by moving the lowest model level closer to the ground. In E2014 it was found that the MetUM 1.5 km performed very well in reproducing the key features of foehn flow across the AP during case A. The MetUM 1.5 km was initiated at 0600 UTC (note local time is three hours behind UTC) on 4 February 2011 and 15 November 2010, for cases A and C respectively, and nested within a regional model with 4 km grid spacing initiated 6 h earlier. This MetUM 4 km model was in turn nested within a global model (with 25 km grid spacing). The majority of analysis presented is from the MetUM 1.5 km runs. However, MetUM 4 km output is used to examine the orographically undisturbed upwind conditions (as the MetUM 1.5 km domain does not extend far enough west of the AP) and to briefly examine the flow response and model performance at a lower resolution. Further details on the model are provided by E2014 and in Orr *et al.* (2014), who use the same configuration.

Using MetUM 1.5 km data as input, air-parcel trajectories have been calculated for each case, using the trajectory model Lagranto

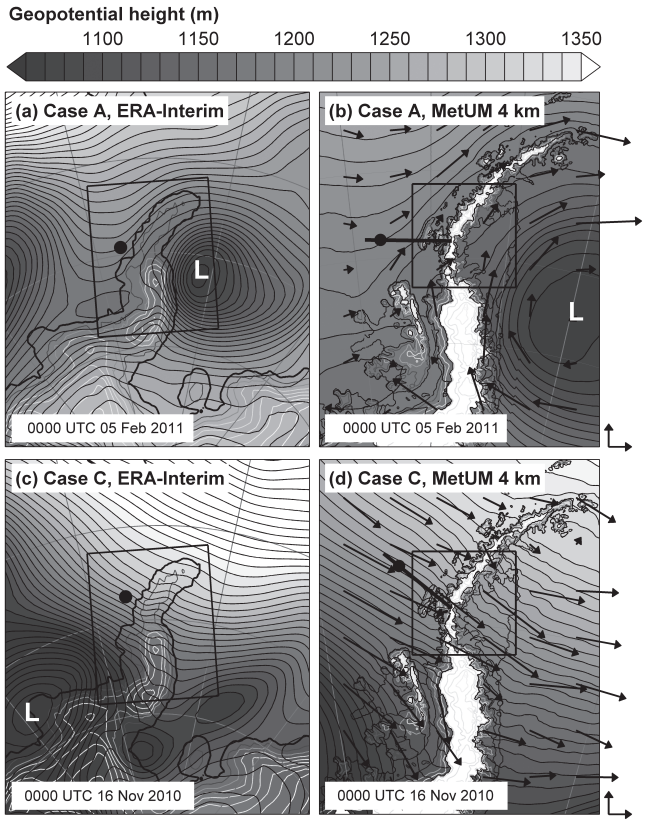

Figure 2. Geopotential height (contours, spaced at 15 m) at the 850 hPa level, from (a,c) the ERA-Interim reanalysis and (b,d) the MetUM 4 km simulation: at (a,b) 0000 UTC on 5 February 2011 during case A, and (c,d) 0000 UTC on 16 November 2010 during case C. Also plotted in (b) and (d) are wind vectors at the 850 hPa level; for scale, vectors to the bottom right of (b) and (d) correspond to 8 m s^{-1}. The black dots mark the locations 150 km upwind of the AP for which upwind model diagnostics are calculated. The black lines in (b) and (d) are the transect lines used for the Figure 3 cross-sections. The inner boxes in (a) and (c) show the region illustrated in (b) and (d), while the inner boxes in (b) and (d) show the MetUM 1.5 km domain.

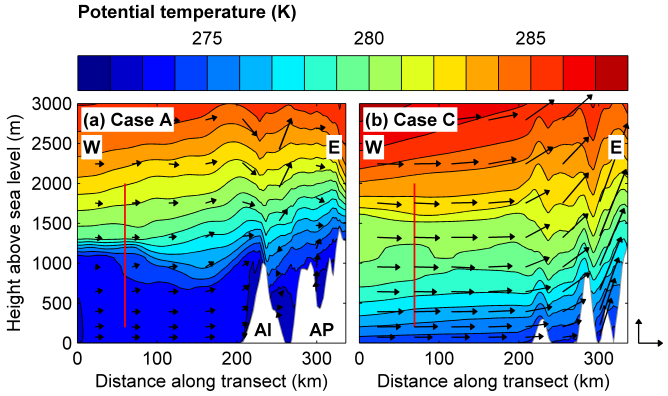

Figure 3. Cross-sections of potential temperature (contours, spaced at 1 K) and along-transect wind vectors at (a) 0000 UTC on 5 February 2011 during case A and (b) 0000 UTC on 16 November during case C. The positions of the cross-sections are shown in Figure 2(b) and (d) respectively. The red vertical line marks the sounding position (~150 km upwind of Adelaide Island, AI) and the depth over which upwind model diagnostics are calculated. Orography is in white (AP, Antarctic Peninsula). For scale, the vectors to the right of the plot correspond to 20 m s^{-1} in the horizontal and 0.2 m s^{-1} in the vertical. The vertical to horizontal scale of axes is 1:100.

(Wernli and Davies, 1997). For the back trajectories shown in this study, Lagranto is run backwards in time for a period of 24 h (more than sufficient considering the size of the MetUM 1.5 km domain) and with a time resolution of 3 min (such a small time step was necessary due to the high spatial resolution).

3.2. *Identification of case studies*

Between 4 and 5 February 2011 a westerly foehn event was observed with aircraft measurements. This short-lived event was characterized by a highly nonlinear flow regime, and is named *case A* (following E2014). The second case addressed in this study, *case C* (15–17 November 2010, following E2014), occurred earlier during the same summer season towards the end of an extended (over 1 month) period of broadly northwesterly foehn during October–November 2010. As well as in E2014, this event has been examined – with a focus on surface energy balance on the LCIS – in Kuipers Munneke *et al.* (2012). There are no airborne observations available for this period, although the generally good performance of the MetUM 1.5 km model in the reproduction of westerly foehn here (case A) and in E2014 gives us confidence in using the model alone to examine the dynamics of case C.

4. Synoptic situation and upwind conditions

4.1. *Case A*

During case A a low-pressure system to the east and a high-pressure ridge to the west of the AP are evident in ERA-Interim reanalysis data (Dee *et al.*, 2011) and the MetUM 4 km simulation (Figure 2(a,b)). At 0000 UTC on 5 February 2011 this is associated with southwesterly flow over the AP upwind of the LCIS (Figure 2(b)). Figure 3(a) shows a west–east cross-section of MetUM 4 km simulated potential temperature (θ) and wind vectors along a cross-section extending roughly 200 km upwind of Adelaide Island. Westerly wind vectors over the mountains show that at least some of the approaching southwesterly flow passes over the AP. Note that the flow field shown in this cross-section is largely representative of flow upwind of the LCIS south of about 67°S (i.e. south of the AP's 'bend'; Figure 1), above which the majority of cross-Peninsula flow passes during case A (as implied by the back trajectories shown later). Little vertical wind shear is apparent, although there is significant vertical variability in $\partial\theta/\partial z$, with a strong inversion particularly apparent at and beyond $\lambda_R \approx 150$ km upwind of the AP, between about 1100 and 1300 m. Similar upwind inversions are also evident in aircraft observations during flights on the afternoon of 4 February and the morning of 5 February (see Figure 4(a) in E2014). As mentioned in section 2, elevated inversions are known to enhance the nonlinearity of cross-barrier flow.

The evolution of upwind conditions during case A is illustrated in Figure 4(a), which shows time series of upwind flow speed and $\hat{h}$ from the MetUM 4 km simulation. These values are vertically averaged (between 200 and 2000 m; considered to be representative of the flow impinging on the AP), at a location $\lambda_R \approx 150$ km west of the AP (location marked on Figures 2(a,b) and 3(a)), and use the westerly component of flow, i.e. that which is roughly perpendicular to the AP south of ~67°S. During the morning and afternoon of 4 February $\hat{h}$ steadily decreases to a minimum of 2.7 at 2100 UTC in association with increasingly westerly winds as the low-pressure centre east of the AP moves south, while the high-pressure ridge west of the AP proceeds east. After this time the winds slacken and $\hat{h}$ increases, bringing to an end the relatively transient, nonlinear ($\hat{h} \gg 1$) partially blocked flow regime that defines case A.

The synoptic-scale situation in the MetUM 4 km compares well with that in ERA-Interim. Note also that E2014 found the MetUM 1.5 and 4 km to produce very similar simulations upwind and, via comparison with aircraft data, perform very well in their reproduction of upwind flow speed and direction, and adequately in their reproduction of upwind static stability. The similarity in upwind conditions between the two simulations supports our use of MetUM 4 km data to help diagnose upwind conditions and relate to downwind conditions in the MetUM 1.5 km simulation.

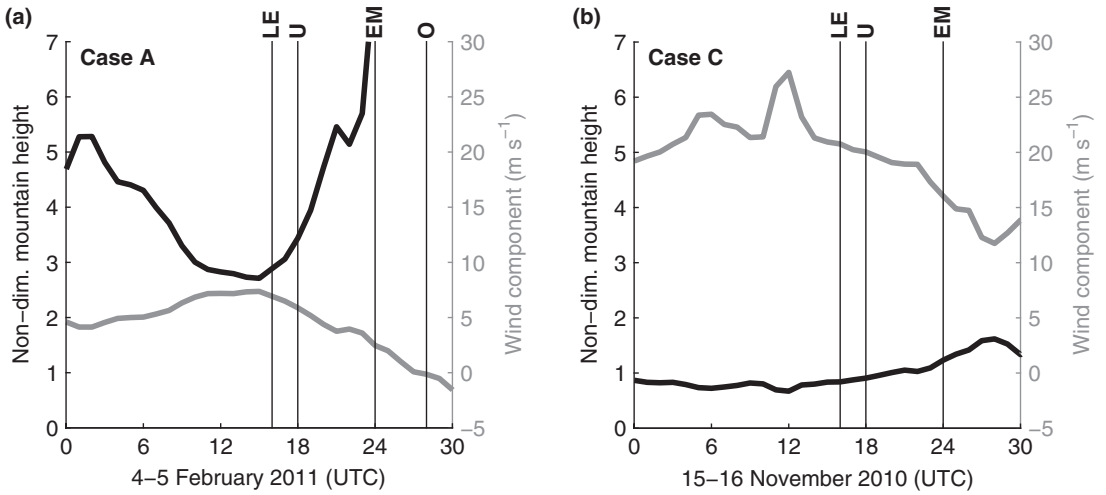

Figure 4. Non-dimensional mountain height (black) and wind-speed component (grey) representative of undisturbed upwind flow for (a) case A and (b) case C. Vertical lines mark key times: LE, *late evening*; EM, *early morning*; U, upwind and synoptic situation (cf. Figures 2 and 3); and O observations (cf. Figures 5(a–c) and 6). Note there are time lags of approximately 10 h for case A and 4 h for case C between undisturbed upwind and lee-side conditions.

4.2. Case C

During case C a deep low-pressure system resides to the southwest of the study area, with large synoptic-scale pressure gradients driving strong northwesterly winds across the length of the AP (Figure 2(c,d)). The strong northwesterlies persist throughout the period of focus (Figure 4(b)), associated with much lower values of $\hat{h}$ than in case A ($\hat{h} < 1$ throughout 15 November 2010, reaching a minimum of 0.67 at 1800 UTC, coincident with a peak northwesterly wind component of $\sim$27 m s^{-1}). Note that $\hat{h}$ in this case is calculated using the northwesterly component of flow, i.e. that which is roughly perpendicular to the AP north of $\sim$67°S (across which the bulk of cross-Peninsula flow passes). A northwest–southeast cross-section of wind vectors and θ reveals little vertical wind shear above the boundary layer and a relatively uniform gradient in θ (and thus N) with height (Figure 3(b)). In contrast with case A, there is no elevated upwind inversion. Wind vectors show northwesterly flow rising over the AP's windward slopes. In short, case C is characterized by a linear flow-over regime, as opposed to the nonlinear partially blocked regime of case A.

5. Lee-side response of the lower atmosphere

5.1. Case A

Figure 5(a–c) shows plan plots of MetUM 1.5 km simulated wind velocity, temperature and specific humidity (q) respectively, at 150 m above mean sea level (AMSL) at 1000 UTC on 5 February 2011. This time coincides with available aircraft observations and captures the event after it has fully evolved (the foehn flow having now advected right across the LCIS). The strength of the flow above the AP's crest at this time is only marginally below its peak earlier that morning (at $\sim$0600 UTC). The major features present at this time are generally representative of the event as a whole. The plot height of 150 m is chosen to represent low level conditions whilst being sufficiently elevated to minimize the effect of diurnal variation in surface temperature and aid cross-case comparison.

On the lee-side the flow field is inhomogeneous, with jets appearing downwind of major inlets (Figure 5(a)). These foehn jets are the downwind continuation of gap flows through lower sections of the AP's crest and are investigated in detail in E2014. Within the jets in Figure 5(a) wind speeds reach in excess of 20 m s^{-1}, defining wind storms that are greatly accelerated relative to the upwind flow (generally $<$10 m s^{-1}). Jet wind speeds are greatest close to the mouths of inlets and subside with distance downwind over the LCIS. Between the jets are regions of calmer or stagnant flow, referred to as 'wakes' here. Near-surface air in the wakes is also foehn air, i.e. derived from west of the AP (E2014). After arriving at the foot of the lee slopes, this air tends to rise and dissipate rather than continue eastward across the LCIS as the jets do (apparent from trajectory analysis, not shown).

Close to the AP, lee-side temperatures are greater and humidities are lower than upwind of the AP (Figure 5(b,c)). The warmer, drier conditions to the east of the AP, in association with the westerly cross-Peninsula flow, attests to the occurrence of a westerly foehn event. Close to the Peninsula's eastern slopes at a latitude of $\sim$67°S, near-surface temperatures (as measured at the lowest flight levels) were observed to increase by $\sim$3.5 K during three consecutive flights over an 18 h period between mid-afternoon on 4 February and early morning the following day (figure 4 in E2014), despite the effect of nocturnal cooling.

In case A, owing to the nonlinearity of the event, the dominant mechanism for foehn warming and drying is the drawdown of air from aloft, associated with upwind blocking of lower level flow (as discussed in E2014). The warmest temperatures, found near the base of the AP's lee slopes are $\sim$10 K greater than the coolest upwind temperatures in the domain (found within Marguerite Bay; see Figure 1(a) for location). The maximum cross-Peninsula difference in q is $\sim$2 g kg^{-1}. The jets are generally cooler and moister than the surrounding foehn air (within the wakes), due to lower upwind source regions (see E2014).

5.2. Case C

Figure 5(d–f) shows the equivalent fields for case C at 2200 UTC on 15 November 2010. These plots also capture the foehn event as flow over the AP's crest is approximately at its strongest. Note some caution should be applied in making cross-case comparisons using these plots due to the different times: the early morning case-A plots will exhibit a more nocturnal signature than the late evening case-C plots.

The foehn effect is again clear, with lee-side temperatures being greater (by a maximum of $\sim$6.5 K) and humidities smaller (by a maximum of $\sim$1.5 g kg^{-1}) than upwind. This time the foehn mechanism largely responsible for these cross-Peninsula gradients is orographic precipitation, causing latent heat gain and moisture loss, as air rises and crosses the mountains (E2014). Note that for both temperature and (more so) humidity, peak cross-Peninsula gradients are greater in case A than case C. Foehn jets are again apparent in the MetUM 1.5 km simulation. These jets are stronger

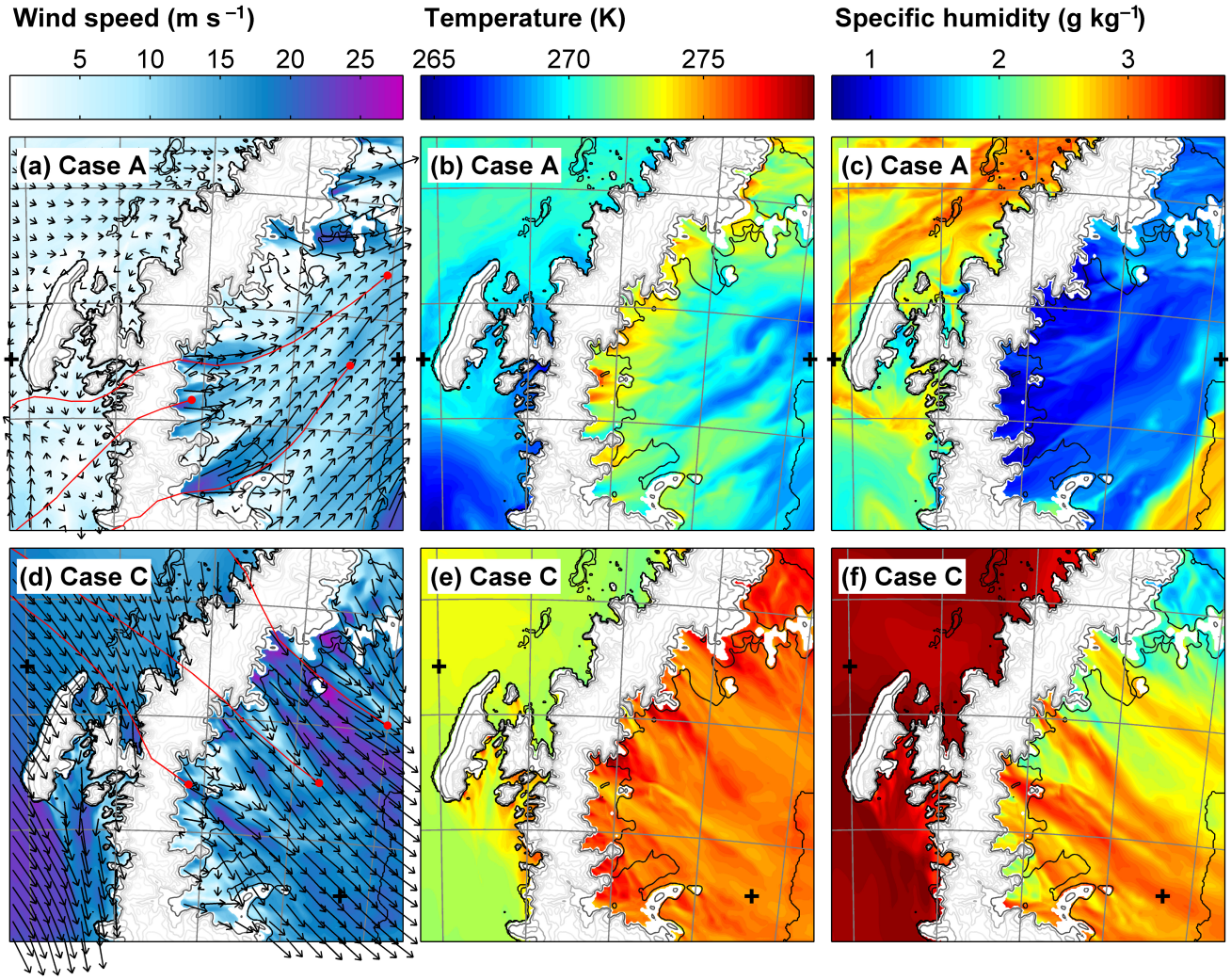

Figure 5. Plan plots of (a,d) wind speed and vectors – with three representative back trajectories initiated on the lee-side at the red circles; (b,e) temperature; and (c,f) specific humidity all at 150 m AMSL. Panels are at (a–c) 1000 UTC on 5 February 2011 during case A and (d–f) 2200 UTC on 15 November 2010 during case C, from the MetUM 1.5 km simulation. Coloured shading is absent where orography exceeds 150 m AMSL. The '+' symbols mark the start and end points of the transects used for the cross-sections of Figures 8 and 9.

(reaching speeds in excess of 25 m s^{-1}) and broader (up to 60 km in cross-sectional width) than in case A. However, the strength of the flow approaching the AP was far greater in case C (generally between 10 and 25 m s^{-1}, in contrast with <10 m s^{-1} during case A), such that the jets are in fact less strongly accelerated across the AP than in case A. Again, the jets are cool and moist relative to the neighbouring wakes, although this time due to reduced diabatic warming as air rises over the AP's windward slopes (see E2014).

5.3. *Lee-side structure: differences between cases A and C*

Figure 5(b) shows a sharp west–east gradient in low-level temperature over the LCIS during case A; the foehn warming effect diminishing with distance downwind of the AP. This structure is confirmed in aircraft observations taken at approximately the same time (~1000 UTC, or 0700 local time, on 5 February 2011) during a 'sawtooth' flight leg (ascending and descending by turn between the near-surface and a higher level) along 67°S (see Figure 1(a) for flight track). Figure 6(a) shows a cross-section of θ interpolated horizontally from this leg. The warm foehn air encroaching from the west is clearly visible, with temperatures over 0 °C observed at near-surface level. Moving east along the leg, near-surface temperatures drop, associated with a deepening and strengthening stable (nocturnal) boundary layer over the ice shelf. The contrast between the warm anomaly induced by the foehn effect close to the AP and the cold pool leads to a horizontal gradient in near-surface temperature of ~10 K over 60 km. Although the MetUM 1.5 km captures the incursion of warm foehn air from the west, it overestimates near-surface temperatures further east, i.e. it underestimates the strength of the surface inversion and the depth of the stable boundary layer. Note that no clear lee-side west–east near-surface gradient in q is apparent over the LCIS in either observations (not shown) or the model (Figure 5(e)). Note the moist southwesterly flow in the southeastern corner of the model domain is inferred to be sourced from east of the AP rather than being foehn air.

For case C, in Figure 5(d,e) the greatest lee-side temperatures are also close to the base of the AP's eastern slopes within the wake regions. In contrast to case A, however, downwind of the major lee-side inlets (i.e. within the jets) temperatures (and humidities) vary little with distance downwind over the LCIS. Again there is no clear downwind gradient in q above the LCIS, apart from where wake regions are interrupted downwind by the divergence of jets.

Figure 7 shows a temperature anomaly for lee-side air above the LCIS at model level 1 (ML1, ~2.5 m) during cases A and C at two different times: *late evening* at 2200 UTC on 4 February 2011 and 15 November 2010 and *early morning* at 0600 UTC on 5 February 2011 and 16 November 2010. The anomaly is calculated as the difference between the *in situ* air temperature at ML1 and the mean temperature of air at the same height over the entire area of the LCIS appearing in the MetUM 1.5 km domain. By removing

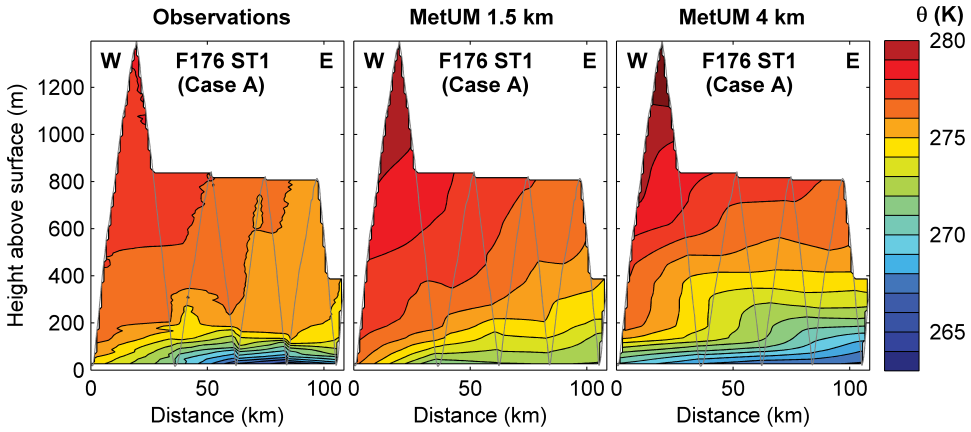

Figure 6. Cross-sections of potential temperature, θ (contours, spaced at 1 K) for the flight 176 sawtooth flight leg between 0900 and 1000 UTC on 5 February 2011 during case A. (a) Shows the aircraft observations; (b) shows MetUM 1.5 km output; and (c) shows MetUM 4 km output. Model data are interpolated in four-dimensions to the flight track. The cross-section is approximately west–east (see Figure 1(a)) with distance marked from the most westerly point. The grey line denotes the flight path.

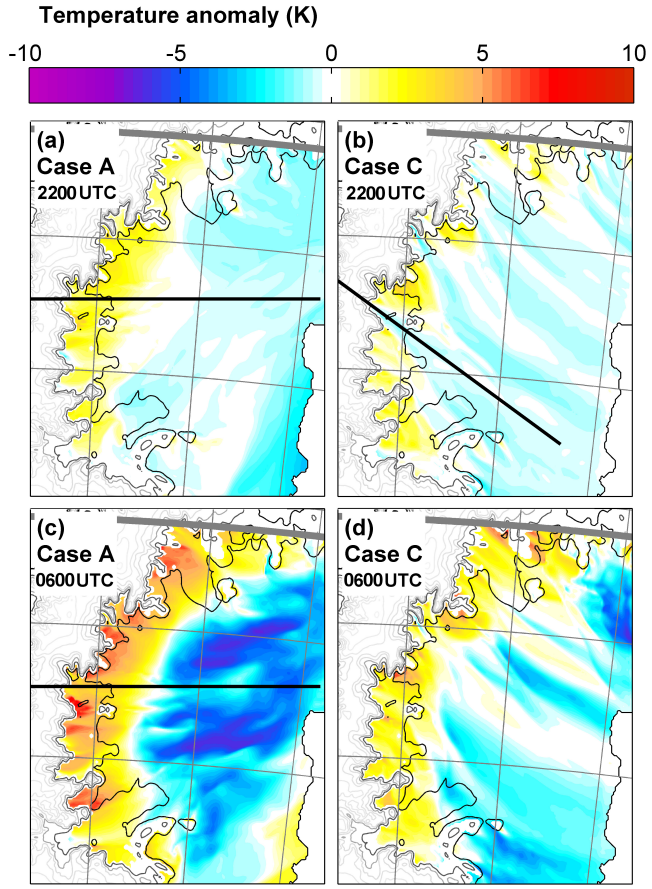

Figure 7. Temperature anomaly above the Larsen C Ice Shelf (LCIS) at ~2.5 m during (a,b) *late evening* and (c,d) *early morning* during (a,c) case A and (b,d) case C. The times for each plot are (a) 2200 UTC on 4 February 2011, (b) 2200 UTC on 15 November 2010, (c) 0600 UTC on 5 February 2011, and (d) 0600 UTC on 16 November 2010. The northern boundary of the LCIS is approximated to be along the 66.2°S line of latitude (thick grey line). Values for locations not above the LCIS are not plotted. The eastern parts of the transects used for the cross-sections in Figures 8 and 9 are marked (black lines).

differences in absolute temperature, these plots are intended to facilitate easier comparisons of lee-side temperature distributions between the two cases and for two times of day.*

The *late evening* plots of Figure 7 reveal the same patterns described briefly above. For case A a relatively simple west–east temperature gradient is apparent, with a band of relatively warm air close to the AP at the near-surface level (defining a west–east temperature difference across the LCIS of 3–4 K). For case C, Figure 7(b) confirms the absence of a general downwind lee-side temperature gradient, with anomalously warm regions close to the base of the lee slopes only in the wake regions. Note that at this time case C is fully evolved, whereas case A is still developing as a foehn event. As such some of the relatively cool air towards the east of the LCIS during case A in Figure 7(a) is not foehn-derived, but sourced from the south, recirculated as part of the low-pressure system to the southeast (Figure 2(a)).

By *early morning* case A is fully evolved with virtually all air above the LCIS being foehn air recently derived from west of the AP (see back trajectories in Figure 5(a)). The same lee-side downwind temperature gradient is apparent, although much amplified (defining a west–east temperature difference of up to 17 K). For case C, a weak (far weaker than in case A) downwind near-surface temperature gradient is now apparent, although within the jets – flowing in a southeasterly direction from WI, Mill Inlet and Cabinet Inlet – this gradient is small or non-existent.

5.4. *Cross-peninsula flow dynamics*

As established above, during the nonlinear case A lee-side drying extends all the way across the LCIS, but lee-side warming diminishes downwind of the AP. In the more linear case C, significant lee-side warming as well as drying extends all the way across the LCIS.

To investigate this further, Figure 8 presents cross-sections derived from the MetUM 1.5 km simulations for both cases at the *late evening* time (cf. Figure 7). In each case these cross-sections pass through the WI jet region in the direction of the prevailing flow and are generally representative of jet-transecting conditions along the length of the AP. They illustrate many of the key differences between the nonlinear (case A) and linear (case C) flows, and provide dynamical insight and explanations for the differences in lee-side warming distributions discussed above.

*There are two notable caveats regarding cross-case comparisons here. Not only do the *late evening* and *early morning* plots capture the events at different stages in their evolution (see Figure 4), the cases occur at different times on the solar calendar. Case C occurred one week closer to the southern solstice than case A, reflected in it being characterized by shorter nights (5.7 and 4.1 h between sunset and sunrise for cases A and C respectively) and greater incoming radiation during the day. The 'foehn clearance' is apparent in both cases, with lee-side conditions entirely cloud-free above the foehn, a feature that enhances the sensitivity of lee-side conditions to changes in radiation. Although inevitably having an important influence on the lee-side conditions during each case, these differences in incoming radiation are unlikely to have a major effect on the qualitative differences between the cases. Note the *early morning* time captures both events before sunrise, after 4.1 and 3.8 h of night-time for cases A and C respectively.

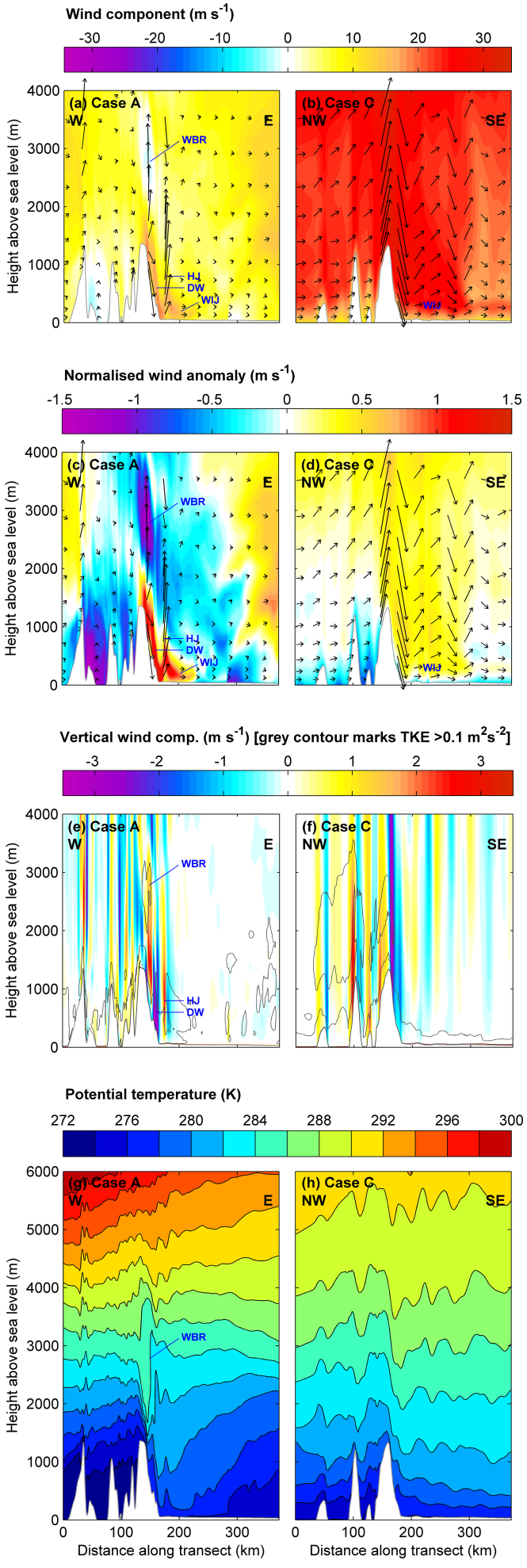

For case A at *late evening*, the cross-sections show many cross-barrier flow phenomena symptomatic of a nonlinear flow regime, including (see Figure 8, left column):

- A region of flow reversal associated with isentropic overturning and turbulence indicated by considerable turbulent kinetic energy (TKE) above the peninsula, all indicating *low-level wave breaking* at a wave-induced critical level at ∼3000 m. The wave breaking is also apparent in the sudden decrease in mountain wave amplitude above this level.
- Strongly accelerated plunging flow above the lee slopes in the form of a *downslope windstorm*.
- Abrupt reascent of flow from the base of the lee slopes, akin to a *hydraulic jump*. This region is characterized by significant TKE. Downwind of the hydraulic jump, some accelerated flow descends to reach the near-surface level and form the WI foehn jet.

For case C the cross-sections generally show a more laminar, linear flow response, with the orography having a weaker influence on the flow field. This linearity is reflected in greater positive vertical velocities above the windward slopes, indicating air rising over the AP. Above and in the lee of the mountains, larger amplitude vertical velocities are simulated for case C than case A. Normalizing vertical velocities by horizontal wind speeds (giving the flow angle from the horizontal), however, produces values for case C that are significantly smaller than case A (not shown), again consistent with the more linear flow regime. No flow reversal, isentropic overturning or upward wave dampening above the mountains indicates an *absence* of wave breaking, and although there is some flow acceleration in the lee of the AP (forming the WI foehn jet; Figure 8(d)), peak normalized wind anomalies (as well as peak absolute wind anomalies, not shown) are smaller than for case A. In further contrast to case A, this positive flow anomaly does not 'hug' the lee slopes to near-surface level over the ice shelf, but is vertically deeper and extends further east above the LCIS. Weak reascent downwind of the AP seems to be associated with a train of horizontally propagating lee waves rather than a hydraulic jump, given the repeated oscillations in vertical wind and θ far downwind of the AP.

For both cases the foehn warming effect is apparent in the θ cross-section (Figure 8(g,h)). In case A, the isentropes plunge steeply downwards immediately east of the AP (reflecting the strong downslope winds), causing a large warm anomaly close to the base of the lee slopes. East of here, the isentropes rise (reflecting the hydraulic jump), such that lower-level temperatures decrease with distance away from the AP – as evident in Figures 5–7. In contrast, in case C the peak foehn warming anomaly is smaller than the high-amplitude warming immediately downwind of the AP, however, isentropes in the lee of the AP are generally flat (or even continue to slope downwards in an easterly direction) at low level over the LCIS. In case C, boundary-layer turbulence associated with vertical wind shear accompanies the warming, affecting the entire ice shelf. This is in contrast to case A, where boundary-layer turbulence above the LCIS is generally confined to the warm region within 50 km of the AP. This relationship between boundary-layer turbulence and temperature demonstrates the effectiveness of wind-shear-driven turbulence within the foehn

Figure 8. Cross-sections of (a,b) horizontal wind component (colour) and vectors (arrows), (c,d) normalized horizontal wind-component anomaly (u', see below), (e,f) vertical velocity and turbulent kinetic energy (grey contours mark values over 0.1 m^2 s^{-2}) and (g,h) θ (contours, spaced at 2 K) during *late evening* at (a,c,e,g) 2200 UTC on 4 February 2011 during case A and (b,d,f,h) 2200 UTC on 15 November 2011 during case C. Output is from MetUM 1.5 km data along a transect passing through WI (see Figure 5 for transects). To calculate u', the vertically averaged upwind along-transect wind component ($\bar{u}$; averaged between 0 and 4000 m at the westernmost point along each transect) is subtracted from the wind field, then normalized by $\bar{u}$. Features highlighted are: WBR, wave braking region; DW, downslope windstorm; HJ, hydraulic jump; WIJ, Whirlwind Inlet jet. The vertical to horizontal scale of axes is 1:100.

flow in maintaining a well-mixed boundary layer and preventing the development of a nocturnal surface inversion above the ice.

By *early morning* the foehn air has advected right across the LCIS in case A.† The key nonlinear features – wave breaking, downslope windstorm, hydraulic jump – are still present and occur at very similar locations (the flow feature labels are in the same position in Figures 8 and 9), which demonstrates the relatively steady-state nature of the cross-barrier flow. Again, a region of enhanced TKE is apparent close to the AP. To the east the isentropes slope upwards away from the AP, confirming the large near-surface west–east temperature gradient evident at the same time in Figure 7(c) and 4 h later in Figures 5(b) and 6, with a strong nocturnal surface inversion east of about 220 km along the transect (Figure 9(e)).

Characteristics of the cross-peninsula flow during case A are revealed in aircraft observations above the AP from flight 177. The aircraft flew four straight and level legs at mean heights of 2620, 2910, 3630 and 4380 m AMSL between 1400 and 1700 UTC 5 February. Fluctuations in westerly wind component u, vertical velocity perturbation w' and potential temperature θ over the AP reveal a clear vertically propagating gravity wave (Figure 10). Above the AP's upper lee slopes a positive θ perturbation of ~2 K was observed during the two lowest flight legs, in accordance with the drawdown of isentropes within the wave at these heights shown in Figure 9(e). Note this perturbation occurs slightly further downwind in the lower of these two flight legs, reflecting the fact that for vertically propagating gravity waves, lines of constant phase tilt upwind (Smith, 1979). The model captures these θ perturbations, reproducing their amplitude and position with reasonable accuracy (Figure 10(c)). The mountain wave's upwind phase tilt is also apparent in the model output along the flight legs and at heights 500 and 1000 m below the lowest flight leg.

More evidence of wave breaking is apparent in observed excursions in u above the lee slopes. For the two lowest flight legs, above the windward slopes u is ~10 m s^{-1} in both the observations and the model. Downwind of the AP's crest a sudden deceleration occurs – more pronounced in the observations than in the model – with the cross-peninsula flow stagnating and even reversing in the observations along the 2910 m leg. The deceleration is not apparent in the two highest flight legs. This agrees remarkably well with the model: although underestimating the amplitude of the deceleration along the two lowest flight legs at the precise times and locations of the observations, a similar region of stagnation and flow reversal is evident between ~2200 and 3500 m in Figure 9(a), and simulated wind-speed perturbations in the horizontal are greatly dampened for the two higher flight legs (Figure 10(a)). As explained above, this is evidence of a wave-induced critical level between around 3000 and 3500 m, and confirms the nonlinear nature of case A.

Observed w' amplitudes above the lee slopes during the two lowest legs are greater than in the model, peaking at approximately ±4 m s^{-1}, in contrast with simulated values of ±1 m s^{-1}. In the two highest flight legs, there is no clear positive θ perturbation, and w' amplitudes are considerably smaller. This is in qualitative agreement with the model and, as above, implies wave breaking.

Observations of TKE (calculated for 3 km run lengths, which matches the resolution of model output sub-grid scale TKE) above the lee slopes in the region of the vertically propagating mountain wave indicate values up to ~5 m^2 s^{-2}, which subside with height. The model fails to replicate the observed peaks in TKE at this time. However, at 500 and 1000 m below the lowest flight-leg observations, or at a time 2 h before the observations (black lines in Figure 10(d)), peaks in simulated TKE are apparent and are the same order of magnitude as those observed. Above the lee slopes downwind of the major mountain wave, particularly large values of TKE are thought to be associated with wave breaking in the region of flow stagnation. The model fails to capture the extent and amplitude of this turbulence, even at the earlier time: note that this subgrid scale TKE from the model is a product of the gravity-wave drag scheme (e.g. Webster *et al.*, 2003).

In general the model performs well in the reproduction of the observed mountain wave structure and breaking. From the two model lines below the lowest flight legs in Figure 10 it is apparent that the simulated wave's amplitude subsides too quickly with height. Equivalent model plots at a time 2 h earlier than the observations for all fields (as shown in black for TKE in Figure 10) reveal simulated wave amplitudes closer to those

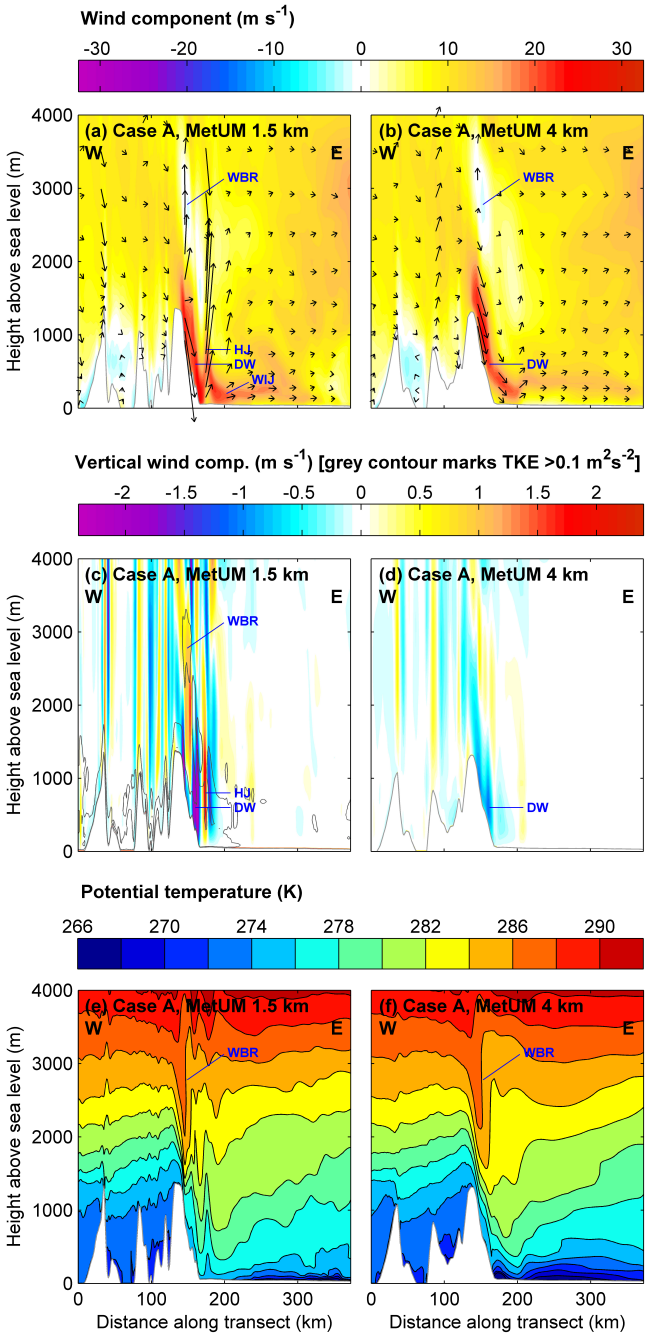

Figure 9. Cross-sections as in Figure 8 but during *early morning* at 0600 UTC on 5 February 2011 during case A comparing (a,c,e) MetUM 1.5 km and (b,d,f) MetUM 4 km simulations. Note that the wind-anomaly panels are omitted and that turbulent kinetic energy (TKE) was not output from the MetUM 4 km model.

†A caveat regarding the case-A cross-sections of Figure 8 is that – as previously mentioned – the foehn event is still developing at this time and is competing with synoptic-scale southwesterlies to the east of the AP. Indeed the foehn front (the transition between foehn air and the non-foehn southwesterly flow to the east) is evident in all the case-A panels of Figure 8 (but not in Figure 9 at the later *early morning* time) at about 280 km along the transect in an abrupt deceleration and ascent of flow, a patch of high TKE and a decrease in θ. The qualitative similarity of the key lee-side features in the case-A panels of Figures 8 and 9 shows that this does not impede our investigation.

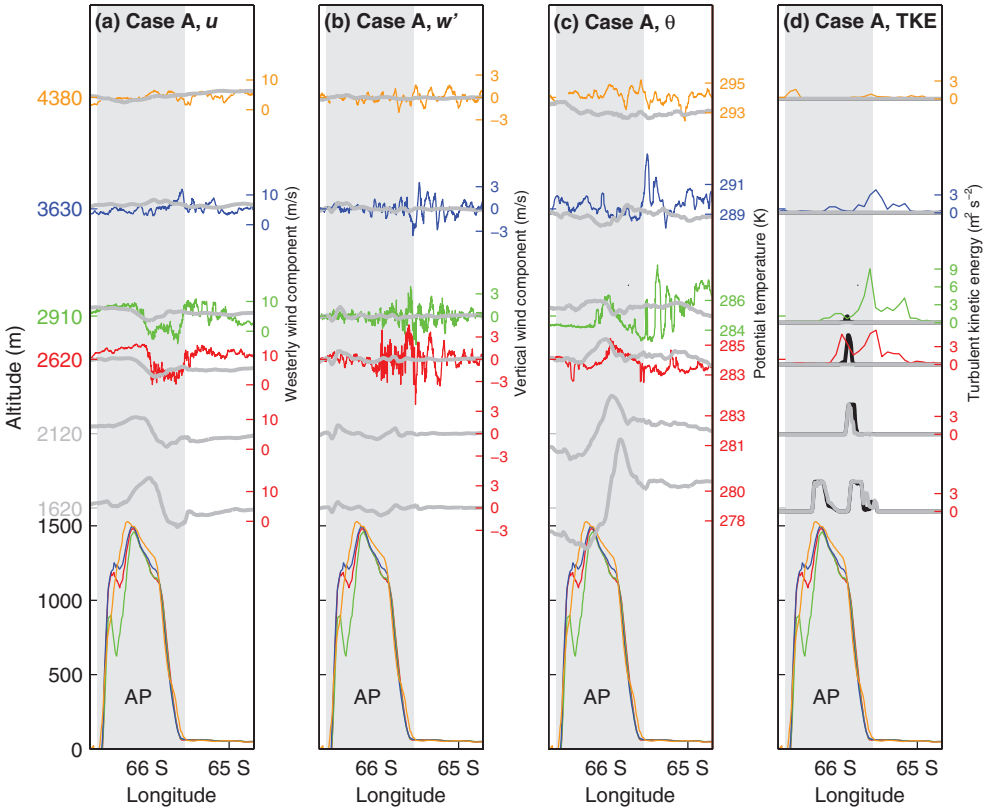

Figure 10. (a) Westerly wind component (u), (b) vertical wind perturbation (w'), (c) potential temperature (θ) and (d) turbulent kinetic energy (TKE) with longitude from aircraft observations during successive roughly west–east, straight and level legs across the AP during flight 177 (between 1400 and 1700 UTC 5 February on 5 February during case A; flight legs are marked on Figure 1). Each traverse is colour coded; the position of each u, w' and θ line corresponds to the mean altitude of the respective flight leg (mean flight altitudes are marked on the left y-axis, to the nearest 10 m), and the orography traversed during each leg is illustrated below the u, w' and θ lines, with the AP marked. Also plotted (thick grey lines) is equivalent MetUM 1.5 km output for each flight leg and at heights 500 and 1000 m below the observations along the lowest flight leg. Additionally, model output at a time 2 h before the observations are plotted (thick black lines) for TKE only. The grey shaded area marks the region in the same vertical plane as the AP.

observed, suggesting that a small model timing error may be largely responsible for this discrepancy.

Above the LCIS, downwind of the sections of the flight legs above the AP, larger amplitude and higher frequency fluctuations in θ are observed, especially in the two middle-altitude flight legs. High frequency fluctuations in u and w' and high levels of turbulent kinetic energy are also observed here. These lee waves and their associated turbulence are *not* resolved by the model, as their wavelengths are simply too small. Neither are they parametrized, as illustrated by the model TKE in Figure 10 and the subgrid-scale sensible heat fluxes (not shown).

5.5. *Discussion*

Cases A and C define two very different foehn regimes across the AP, with marked differences in lee-side response above the LCIS. The nonlinear case A exhibits a larger amplitude lee-side foehn warming effect in the immediate lee of the AP: the more strongly accelerated downslope foehn winds – associated with upwind flow blocking and the drawdown of potentially warm air from aloft – induces a greater positive lee-side temperature anomaly than the latent heating foehn mechanism of case C. Conversely, downwind of the AP the foehn warming effect rapidly diminishes across the ice shelf, whereas in case C the stronger lee-side winds and linear flow regime lead to a more extensive warming, still apparent over 200 km downwind of the mountains. Thus, across the LCIS there is a greater temperature gradient in case A than during case C. This is particularly apparent after night-time cooling, when a strong surface inversion develops over all but a relatively narrow strip close to the AP's eastern slopes. In case A the warm, turbulent foehn descends towards the base of these slopes, acting to maintain a well-mixed boundary layer, even during the night. However, the foehn then rises abruptly, in the form of a hydraulic jump, before re-descending sharply to near-surface levels. Consistent with the advection of momentum away from the surface, and energy dissipation imparted by turbulence in the vicinity of the hydraulic jump, the strong winds are weakened in the lee of the jump.

In both cases foehn air reaches the eastern ice-shelf edge at low levels, as is evident from wind vectors and back trajectories (Figure 5(a,d)). Hence the difference in lee-side warming versus drying distribution is due to a sink of heat – namely cooling of air by the ice shelf – as opposed to advective differences. So in case A, downwind of the hydraulic jump, the downward heating due to turbulent mixing is small relative to the loss of heat to the surface (particularly so during the night due to radiative cooling of the ice), dictating a sensible heat flux divergence that leads to downwind cooling at the near-surface level over the LCIS (Figure 7(a,c)).

During case C, near-surface foehn winds are considerably stronger further to the east of the AP over the LCIS. This is to be expected given the greater upwind/background wind speeds and the greater linearity of the flow regime (meaning a weaker cross-barrier drag force applied to the flow, and the absence of a lee-side hydraulic jump). Isentropes are generally flat at low levels during the *late evening* over the entire LCIS, indicating that the heat loss to the ice surface is balanced by the downward heat exchange caused by the turbulent foehn winds (attested to by significant TKE at low level above the LCIS). Indeed at night, the wind-shear-induced mechanical mixing at near-surface level (owing to the strong near-surface foehn winds) is able to prevent the formation of a strong nocturnal inversion, leading to warmer near-surface conditions east over the LCIS (Figure 7(b,d)).

Another mechanism for the decreased foehn effect away from the foot of the mountains is the confinement of the warm, dry wake regions to this area. As previously mentioned, the wake air does not

advect east across the LCIS at low level, rather it ascends and dissipates while the cooler, drier jets progress eastwards and diverge.

6. Model sensitivity

Alongside the MetUM 1.5 km cross-sections, Figure 9 shows equivalent MetUM 4 km cross-sections. Although conditions along vertical profiles upwind of the AP are very similar in the two models, differences in the representation of dynamical processes across and downwind of the mountains result in important differences in their lee-side response. In both simulations strong foehn winds descend the AP's lee slopes, associated with wave breaking (evident above the mountains in the form of a region of flow stagnation/reversal and isentropic overturning, above which wave amplitudes decrease). However, these winds are characterized by far greater vertical velocities and a more pronounced lee-side foehn jet in the 1.5 km model. As discussed above (cf. Figure 10), w' is underestimated in the 1.5 km simulation, which implies that it must be severely underestimated in the 4 km model. Plan plots of low-level winds demonstrate that the 4 km model can simulate foehn jets (cf. Figure 5(a)) but only crudely (not shown). The peak wind speeds are lower and the jets are broader than in the 1.5 km simulation, which is shown in E2014 to do a good job of capturing these jet characteristics when compared to aircraft observations.

The downslope windstorm of the 1.5 km simulation is able to penetrate all the way down to near-surface level, whereas in the 4 km simulation it separates itself from the lee slopes above the ice shelf (Figure 9(b)). This difference is probably responsible for the warmer near-surface temperatures on the lee-side at the base of the AP in the 1.5 km simulation, which are ∼10 K higher than in the 4 km simulation. Another key difference between the two simulations is the appearance of a hydraulic jump in the finer but not the coarser model. Differences in the representation of lee-side conditions over the ice will also be due to any sensitivity to model resolution of parameterized processes such as boundary-layer turbulent mixing (Orr *et al.*, 2014).

Differences in model representation are also demonstrated in Figure 6, which shows θ cross-sections from observations and the simulations. Once again near-surface temperatures are considerably greater in the higher resolution model towards the base of the lee slopes (∼7 K greater at the most westerly point along the leg) and, to a lesser extent, further east over the LCIS (generally ∼4 K greater). Compared to the observations, the MetUM 1.5 km simulation performs better close to the AP, but it is too warm further to the east near the surface of the LCIS, i.e. it fails to reproduce the strong nocturnal stable boundary layer. Note that this is a common failure of numerical weather prediction models in the polar regions (e.g. Cuxart *et al.*, 2006), and does not qualitatively have an impact on the results of our analysis. The overall vertical structure of the lee-side temperature is better in the 1.5 km model, providing a better qualitative simulation than the 4 km model.

In short, a model grid spacing of 1.5 km or smaller is necessary to adequately capture foehn flows over the AP, in particular to accurately reproduce the foehn jets and capture nonlinear features such as hydraulic jumps.

7. Implications for Larsen C Ice Shelf melt

Figure 11 illustrates the model surface energy budgets (SEB), surface (skin) temperatures and melt characteristics spatially averaged over the LCIS (unshaded region in Figure 1, below 100 m) over 24 h beginning and ending at local midday (1500 UTC) for each of the foehn cases. The net surface heat flux is calculated as the sum of the individual SEB components shown (all positive downwards) – we assume that there is no ground heat flux. Previous SEB studies for the LCIS (e.g. van den Broeke, 2005; King *et al.*, 2008; Välisuo *et al.*, 2014) have also assumed that the ground heat flux is small over the ice shelf in summer. Surface temperatures do not surpass 0 °C as at this temperature all additional heat is used for melt, and the model does not account for the formation of surface melt ponds. Melt rates are calculated for each model grid point of the LCIS as the residual positive energy flux *when* the surface is at the melting point.

In both foehn cases the surface variables exhibit clear diurnal signatures, with the shortwave radiative (SW) flux dominating the SEB (Figure 11(a,b)), and melt apparent exclusively during the day (Figure 11(c,d)). Ice melt during foehn conditions is a result of positive SW fluxes due to the 'foehn clearance' of clouds and positive sensible heat (SH) fluxes due to the warmth of the foehn air and strong winds. The consistently greater surface temperatures and net downward surface fluxes during case C are due to greater surface SH fluxes (by 30 W m^{-2} on average) – a result of the warmer foehn air and stronger winds – and, to a lesser extent, greater SW fluxes (by 14 W m^{-2} on average) as this case is closer to the southern solstice. The remaining two components of the SEB – the longwave and latent heat fluxes – cool the surface and generally have greater (negative) contributions to the SEB in case C, but not enough to offset the greater (positive) contributions of the two warming components.

Of all the SEB components, it is the variation in the SH flux that is most pertinent in comparing the different foehn flow regimes. At night, weaker SH fluxes during case A are principally responsible for the rapid fall in surface temperature (to −12 °C) compared with case C (−6 °C). This considerable surface-temperature deficit together with a later sunrise explains the later onset of melt in case A the following morning. In case A during the middle part of the day, convective conditions persist over all, but the westernmost LCIS (where the foehn warming effect is greatest; Figure 5(b)), with negative (i.e. upward) SH fluxes delivering a cooling effect to the ice (a common occurrence over the LCIS in summer; Kuipers-Munneke *et al.*, 2012). In contrast, in case C the SH fluxes remain positive everywhere due to the presence of warm foehn air across the entire ice-shelf surface (cf. Figure 5(e)).

Although the entire ice shelf is melting for several hours during the case-C 24 h period (reflected in the spatially averaged surface temperature being at the melting point), a maximum of only ∼80% of the ice shelf is melting at any one time during case A (owing to easternmost portions of the LCIS remaining cooler than 0 °C throughout). Furthermore, due to greater net surface fluxes, the energy available for melting is generally over twice as great during case C than case A, with melt rates of 4.8 versus 1.7 mm over the respective 24 h periods (note that melt depths here and below are given as water-equivalent, as is standard). A more asymmetric melt distribution during case A is apparent in mean melt longitude (Figure 11(c,d)), with average melt occurring consistently further west in case A than case C (note the mean melt longitude here is for all model grid points over the LCIS and is weighted by the amount of energy available for melt). Also apparent is, in both cases, the progression of mean melt location from west to east in the morning and then regression back to west in the evening, due to the combination of foehn and diurnal forcings.[‡]

The melt rates and distributions computed for our foehn cases are comparable to previous observation- and model-derived climatological estimates of LCIS melt rates. Luckman *et al.* (2014) used Synthetic Aperture Radar to map the spatial distribution of annual melt duration over the LCIS. There is a strong resemblance between their map of melt distribution and our warming and melt distributions – especially for case A – with highest melt durations at the foot of the lee slopes. Van den Broeke (2005) made summer estimates of melt rate using east LCIS automatic weather station (AWS) measurements to determine

[‡]Note that the inconsistently eastern locations of melt at 2100 UTC on 4 February and 1400 UTC on 5 February during case A is due to a small patch of more persistent but much weaker non-foehn-induced melt east of Mobil Oil Inlet.

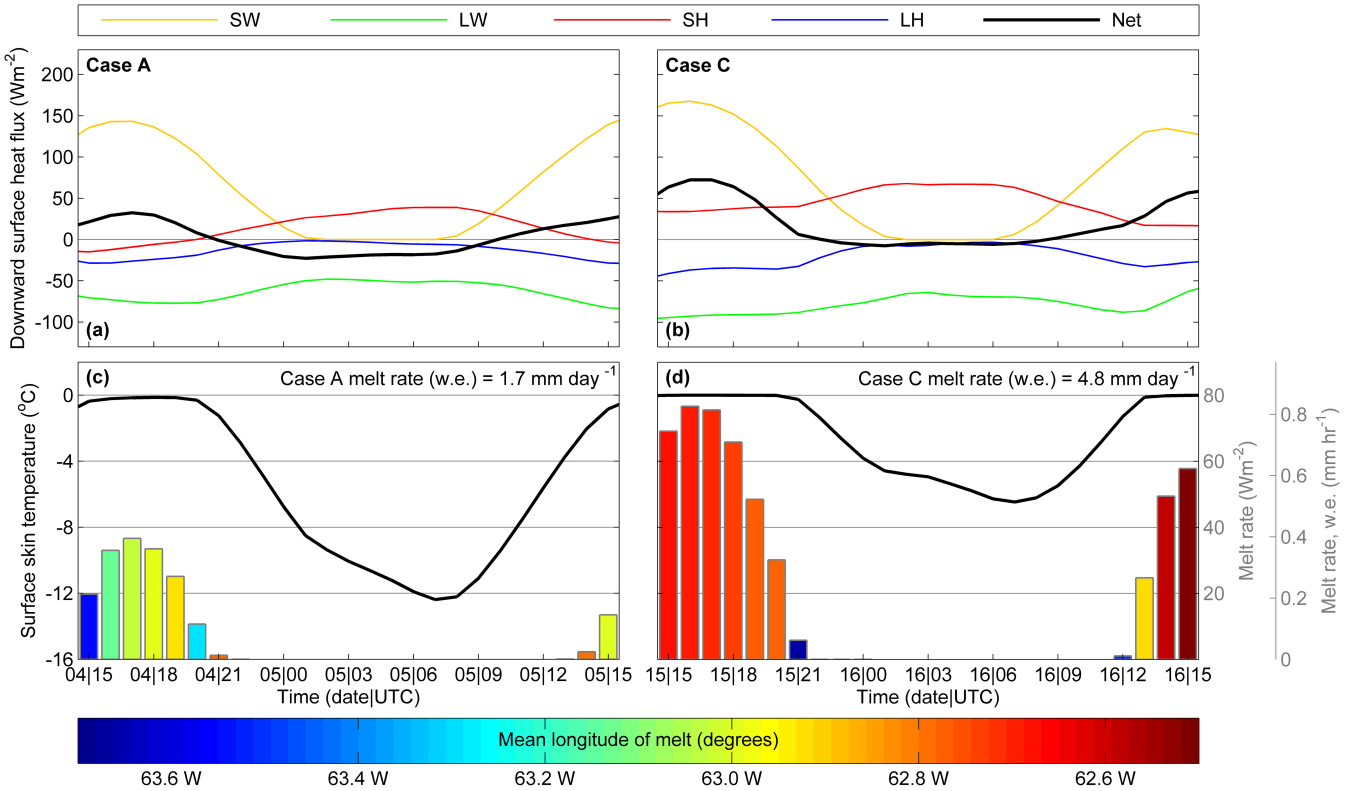

Figure 11. Surface energy budget components (positive downwards) during (a) case A and (b) case C; as well as surface skin temperature (black line) and melt rates (bars) during (c) case A and (d) case C. The melt rates are shown as both an energy flux (W m^{-2}) and a water equivalent (w. e.) melt rate (mm). The shading in the bars indicates the mean longitude of the melting. All other quantities are spatially averaged across the Larsen C Ice Shelf using output from the MetUM 1.5 km simulations. The time series start at 1500 UTC (local midday) and show 24 h.

wind-direction-binned values ranging from 0.5 to 4 mm day^{-1}. Kuipers-Munneke *et al.* (2012) used AWS measurements at the same location (*Larsen Camp*) to determine mean summer melt rates of 2.3 mm day^{-1} between 2009 and 2011 and 7.7 mm day^{-1} over a 9-day foehn period, which includes case C. Välisuo *et al.* (2014) used ERA-Interim reanalysis data to find a summer mean melt rate for the LCIS equivalent to 2.8 mm day^{-1} between 1989 and 2008.

In the context of these climatological values our modelled melt rates for case A (1.7 mm day^{-1}) are modest, whereas those during case C (4.8 mm day^{-1}) are high. The implication is that foehn in linear flow regimes can drive particularly high melt rates over the LCIS. This is accentuated when one considers that: (i) our modelled melt rates appear to be underestimates for case C – implied by comparison with Kuipers-Munneke *et al.*'s (2012) observed melt rate of 7.7 mm day^{-1} (mentioned above; note that this is a point measurement and is for an extended 9-day period) and confirmed in Elvidge (2013), who finds simulated daily melt during case C to be 65% that of AWS observations at *Larsen Camp*; and (ii) case C occurred in early summer when incoming solar radiation was relatively small for the summer melt periods the climatological values are averaged over (note that the same is true for case A, which occurred in late summer). The underestimate in melt rates appears to be largely a result of discrepancies in radiative fluxes owing to misrepresentation of albedo or cloud (according to comparison with AWS data, not shown). For example, our simulated melt estimates do not account for the positive feedback effect of melt ponds, the formation of which bring about a reduction in surface albedo and hence an increase in absorbed SW and melt. Further investigation of this will be the subject of future work.

8. Conclusions and implications

For foehn flows over the AP we have shown that the foehn effect is greatest in the immediate lee of the mountains, due to the confinement of relatively warm, dry wakes to this region and heat loss to the ice surface further downwind. Our findings show this lee-side temperature gradient to be more pronounced in a nonlinear flow regime. This nonlinear event features gravity wave breaking (uniquely observed in aircraft data), a downslope windstorm and a hydraulic jump. Greater foehn warming over the Larsen C Ice Shelf as a whole is associated with a linear flow regime characterized by stronger cross-peninsula winds. In such circumstances the warming extends further downwind because the downward heat exchange caused by the turbulent foehn is great enough to counteract heat loss to the surface across the entire ice shelf. Via a surface energy budget comparison, we have shown that linear flow regimes also induce the greatest melt over the entire LCIS, due to a greater transfer of sensible heat to the surface as a result of the greater coverage of warm, strong, low-level foehn winds over the entire ice shelf. This sensible heat flux prevents surface temperatures from plummeting during the night and aids the large net shortwave fluxes typical of lee-side foehn conditions in warming and melting the ice shelf during the day. The large and systematic variations in the distribution of lee-side temperature, wind speeds and melt rates between our two cases highlight that lee-side flow dynamics, governed by flow-regime linearity, are important in determining the SEB across the ice shelf.

As the AP provides an excellent 'natural laboratory' for the study of foehn, this work also has general implications for the impact of foehn events in other mountainous regions; for example improved understanding of the downwind distribution of foehn warming would help weather forecasting in such regions. Hoinka (1985) briefly discusses the downwind extent of the foehn effect – with reference to the Alps and the Colorado Rockies – stating that the strong, gusty winds often found at the base of the lee slopes are usually absent 50 km further downwind, while the warming and drying effect may extend up to 100 km away from the barrier. Our results show that foehn warming can in fact extend hundreds of kilometers downwind,

and that the phenomenon Hoinka describes is consistent with a nonlinear cross-barrier flow, for which a hydraulic jump deflects the foehn flow upwards. Friction-generated turbulence could also be responsible for the cessation of strong near-surface wind; lee-side topography in the Alps and Rockies generally being significantly rougher than that of the LCIS. As we have found, the lee-side warming distribution depends not just on atmospheric properties but also on surface type and temperature. For example, the surface cooling we see over the LCIS is probably analogous to nocturnal or wintertime cooling at mid-latitudes. Further investigation will be required to fully translate our findings to other regions.

In order to corroborate the conclusions of this study, further aircraft observations and simulations of both nonlinear and linear foehn events are required for the AP and elsewhere. Idealized model analysis would be particularly helpful in clarifying differences in lee-side response in the absence of orographic complexity and diurnal or synoptic variability. Furthermore, to utilize the findings of this study in improving our understanding of the links between westerly foehn across the AP and east-coast climatic warming and ice melt, a climatological analysis of upwind conditions to the west of the AP is required to determine the frequency and intensity of foehn events, their linearity and their associated melt rates.

Acknowledgements

This article was made possible by funding provided by NERC under the OFCAP project grant NE/G014124/1. All members of the OFCAP project, the Field Operations team and others at Rothera Research Station are to be acknowledged for valuable contributions towards the planning, technical and practical aspects of the observational data capture during the field campaign, and subsequent quality control and processing of data. We thank the NCAS team at the University of Reading, M. Weeks, S. Webster and S. Vosper for advice and assistance with running the MetUM, and T. Phillips for providing the orography data. We acknowledge use of the MONSooN system, a collaborative facility supplied under the Joint Weather and Climate Research Programme, which is a strategic partnership between the Met Office and the Natural Environment Research Council. A. Ross and A. Matthews provided useful discussion and comments during the first author's PhD Viva. We thank three reviewers for useful comments that have improved this article – in particular their encouragement to include the SEB analysis.

References

Brinkmann WA. 1974. Strong downslope winds at Boulder, Colorado. *Mon. Weather Rev.* **102**: 592–602.

Clark TL, Peltier WR. 1977. On the evolution and stability of finite-amplitude mountain waves. *J. Atmos. Sci.* **34**: 1715–1730.

Colle BA, Mass CF. 1998. Windstorms along the western side of the Washington Cascade Mountains. Part I: A high-resolution observational and modeling study of the 12 February 1995 event. *Mon. Weather Rev.* **126**: 28–52.

Cook AJ, Vaughan DG. 2010. Overview of areal changes of the ice shelves on the Antarctic Peninsula over the past 50 years. *Cryosphere* **4**: 77–98.

Cuxart J, Holtslag AAM, Beare RJ, Bazile E, Beljaars A, Cheng A, Conangla L, Ek M, Freedman F, Hamdi R, Kerstein A, Kitagawa H, Lenderink G, Lewellen D, Mailhot J, Mauritsen T, Perov V, Schayes G, Steeneveld G-J, Svensson G, Taylor P, Weng W, Wunsch S, Xu K-M. 2006. Single-column model intercomparison for a stably strati?ed atmospheric boundary layer. *Boundary-Layer Meteorol.* **118**: 273–303.

Davies T, Cullen MJP, Malcolm AJ, Mawson MH, Staniforth A, White AA, Wood N. 2005. A new dynamical core for the Met Office's global and regional modelling of the atmosphere. *Q. J. R. Meteorol. Soc.* **131**: 1759–1782.

Dee DP, Uppala SM, Simmons AJ, Berrisford P, Poli P, Kobayashi S, Andrae U, Balmaseda MA, Balsamo G, Bauer P, Bechtold P, Beljaars ACM, van de Berg L, Bidlot J, Bormann N, Delsol C, Dragani R, Fuentes M, Geer AJ, Haimberger L, Healy SB, Hersbach H, Hólm EV, Isaksen L, Kållberg P, Köhler M, Matricardi M, McNally AP, Monge-Sanz BM, Morcrette J-J, Park B-K, Peubey C, de Rosnay P, Tavolato C, Thépaut J-N, Vitart F. 2011. The ERA-Interim reanalysis: Configuration and performance of the data assimilation system. *Q. J. R. Meteorol. Soc.* **137**: 553–597.

Durran DR. 1986. Another look at downslope windstorms. Part I: The development of analogs to supercritical flow in an infinitely deep, continuously stratified fluid. *J. Atmos. Sci.* **43**: 2527–2543.

Durran DR. 1990. Mountain waves and downslope winds. In *Atmospheric Processes Over Complex Terrain*, Blumen W. (ed.) *Meteorological Monographs* **23**: 59–81. American Meteorological Society: Boston, MA.

Elvidge AD. 2013. 'Polar föhn winds and warming over the Larsen C Ice Shelf, Antarctica', PhD thesis. University of East Anglia: East Anglia, UK.

Elvidge AD, Renfrew IA, King JC, Orr A, Lachlan-Cope TA, Weeks M, Gray SL. 2014. Foehn jets over the Larsen C Ice Shelf, Antarctica. *Q. J. R. Meteorol. Soc.*, doi: 10.1002/qj.2382.

Fiedler EK, Lachlan-Cope TA, Renfrew IA, King JC. 2010. Convective heat transfer over thin ice covered coastal polynyas. *J. Geophys. Res.: Oceans* **115**: 1978–2012, doi: 10.1029/2009JC005797.

Garman KE, Hill KA, Wyss P, Carlsen M, Zimmerman JR, Stirm BH, Carney TQ, Santini R, Shepson PB. 2006. An airborne and wind tunnel evaluation of a wind turbulence measurement system for aircraft-based flux measurements. *J. Atmos. Oceanic Technol.* **23**: 1696–1708.

Hoinka KP. 1985. What is a foehn clearance? *Bull. Am. Meteorol. Soc.* **66**: 1123–1123.

Hunt JCR, Snyder WH. 1980. Experiments on stably and neutrally stratified flow over a model three-dimensional hill. *J. Fluid Mech.* **96**: 671–704.

King JC, Lachlan-Cope TA, Ladkin RS, Weiss A. 2008 Airborne measurements in the stable boundary layer over the Larsen Ice Shelf, Antarctica. *Boundary-Layer Meteorol.* **127**: 413–428.

Klemp JB, Lilly DR. 1975. The dynamics of wave-induced downslope winds. *J. Atmos. Sci.* **32**: 320–339.

Kuipers-Munneke P, van den Broeke MR, King JC, Gray T, Reijmer CH. 2012. Near-surface climate and surface energy budget of Larsen C ice shelf, Antarctic Peninsula. *Cryosphere* **6**: 353–363.

Lilly DK. 1978. A severe downslope windstorm and aircraft turbulence event induced by a mountain wave. *J. Atmos. Sci.* **35**: 59–77.

van Lipzig NPM, Marshall GJ, Orr A, King JC. 2008. The relationship between the Southern Hemisphere Annular Mode and Antarctic Peninsula summer temperatures: Analysis of a high-resolution model climatology. *J. Clim.* **21**: 1649–1668.

Long RR. 1953. Some aspects of the flow of stratified fluids: I. A theoretical investigation. *Tellus* **5**: 42–58.

Luckman A, Elvidge AD, Jansen D, Kulessa B, Kuipers Munneke P, King JC, Berrand NE. 2014. Surface melt and ponding on Larsen C Ice Shelf and the impact of foehn winds. *Antarct. Sci.* **26**: 625–635, doi: 10.1017/S0954102014000339.

Marshall GJ, Orr A, van Lipzig NP, King JC. 2006. The impact of a changing Southern Hemisphere Annular Mode on Antarctic Peninsula summer temperatures. *J. Clim.* **19**: 5388–5404.

Mayr GJ, Armi L, Gohm A, Zängl G, Durran DR, Flamant C, Gaberšek S, Mobbs S, Ross A, Weissmann M. 2007. Gap flows: results from the Mesoscale Alpine Programme. *Q. J. R. Meteorol. Soc.* **133**: 881–896.

Natural Environment Research Council, Lachlan-Cope TA, Elvidge AD, Smith V, Kirchgaessner A, King JC, Ladkin R. 2014. British Antarctic Survey Twin Otter aircraft Meteorological Airborne Science INstrumentation (MASIN) core data from the Orographic Flows and the Climate of the Antarctic Peninsula (OFCAP) project (2011), 24 September 2014. NCAS British Atmospheric Data Centre: Didcot, UK, doi: 10.5285/2f53b18d-49fc-4477-b994-f1719d6f6dbe.

Ólafsson H. 2005. The heat source of the foehn. *Hrvatski Meteorološki časopis* **40**: 542–545.

Orr A, Marshall GJ, Hunt JC, Sommeria J, Wang CG, van Lipzig NP, Cresswell D, King JC. 2008. Characteristics of summer airflow over the Antarctic Peninsula in response to recent strengthening of westerly circumpolar winds. *J. Atmos. Sci.* **65**: 1396–1413.

Orr A, Phillips T, Webster S, Elvidge AD, Weeks M, Hosking JS, Turner J. 2014. Met Office Unified Model high-resolution simulations of a strong wind event in Antarctica. *Q. J. R. Meteorol. Soc.* doi:10.1002/qj.2296.

Peltier WR, Clark TL. 1983. Nonlinear mountain waves in two and three spatial dimensions. *Q. J. R. Meteorol. Soc.* **109**: 527–548.

Rignot E, Casassa G, Gogineni P, Krabill W, Rivera A, Thomas R. 2004. Accelerated ice discharge from the Antarctic Peninsula following the collapse of Larsen B ice shelf. *Geophys. Res. Lett.* **31**: L18401, doi: 10.1029/2004GL020697.

Scorer RS. 1949. Theory of waves in the lee of mountains. *Q. J. R. Meteorol. Soc.* **75**: 41–56.

Smith RB. 1979. The influence of mountains on the atmosphere. *Adv. Geophys.* **21**: 87–230.

Smith RB. 1980. Linear theory of stratified hydrostatic flow past an isolated mountain. *Tellus* **32**: 348–364.

Smith RB. 1985. On severe downslope winds. *J. Atmos. Sci.* **42**: 2597–2603.

Smith RB, Grønås S. 1993. Stagnation points and bifurcation in 3-D mountain airflow. *Tellus A* **45**: 28–43.

Smith CM, Skyllingstad ED. 2005. Numerical simulation of katabatic flow with changing slope angle. *Mon. Weather Rev.* **133**: 3065–3080.

Speirs JC, Steinhoff DF, McGowan HA, Bromwich DH, Monaghan AJ. 2010. Foehn winds in the McMurdo Dry Valleys, Antarctica: The origin of extreme warming events. *J. Clim.* **23**: 3577–3598.

Steinhoff DF, Bromwich DH, Monaghan A. 2013. Dynamics of the foehn mechanism in the McMurdo Dry Valleys of Antarctica from Polar WRF. *Q. J. R. Meteorol. Soc.* **139**: 1615–1631.

Trombetti F, Tampieri F. 1987. An application of the dividing-streamline concept to the stable airflow over mesoscale mountains. *Mon. Weather Rev.* **115**: 1802–1806.

Välisuo I, Vihma T, King JC. 2014. Surface energy budget on Larsen and Wilkins ice shelves in the Antarctic Peninsula: Results based on reanalyses in 1989–2010. *Cryosphere* **8**: 1519–1538, doi: 10.5194/tc-8-1519-2014.

Van den Broeke MR. 2005. Strong surface melting preceded collapse of Antarctic Peninsula ice shelf. *Geophys. Res. Lett.* **32**: L12815, doi: 10.1029/2005GL023247.

Vaughan DG, Doake CSM. 1996. Recent atmospheric warming and retreat of ice shelves on the Antarctic Peninsula. *Nature* **379**: 328–331.

Vaughan DG, Marshall GJ, Connolley WM, Parkinson C, Mulvaney R, Hodgson DA, King JC, Pudsey CJ, Turner J. 2003. Recent rapid regional climate warming on the Antarctic Peninsula. *Clim. Change* **60**: 243–274.

Webster S, Brown AR, Cameron DR, Jones CP. 2003. Improvements to the representation of orography in the Met Office Unified Model. *Q. J. R. Meteorol. Soc.* **129**: 1989–2010.

Wernli BH, Davies HC. 1997. A Lagrangian-based analysis of extratropical cyclones. I: The method and some applications. *Q. J. R. Meteorol. Soc.* **123**: 467–489.

Whiteman CD. 2000. *Mountain Meteorology: Fundamentals and Applications.* Pacific Northwest National Laboratory, Oxford University Press: New York, NY.

WMO. 1992. *International Meteorological Vocabulary* (2nd edn), Vol. 182. World Meteorological Organization: Geneva, Switzerland.

Zängl G, Gohm A, Obleitner F. 2008. The impact of the PBL scheme and the vertical distribution of model layers on simulations of Alpine foehn. *Meteorol. Atmos. Phys.* **99**: 105–128.